Interlocking activities of DNA polymerase β in the base excision repair pathway

Adarsh Kumar[a], Andrew J. Reed[b], Walter J. Zahurancik[b], Sasha M. Daskalova[c], Sidney M. Hecht[c], and Zucai Suo[a,b,1]

[a]Department of Biomedical Sciences, Florida State University College of Medicine, Tallahassee, FL 32306; [b]The Ohio State Biochemistry Program, The Ohio State University, Columbus, OH 43210; and [c]Biodesign Center for BioEnergetics and School of Molecular Sciences, Arizona State University, Tempe, AZ 85287

Edited by Graham Walker, Department of Biology, Massachusetts Institute of Technology, Cambridge, MA; received October 27, 2021; accepted January 10, 2022

Base excision repair (BER) is a major cellular pathway for DNA damage repair. During BER, DNA polymerase β (Polβ) is hypothesized to first perform gap-filling DNA synthesis by its polymerase activity and then cleave a 5′-deoxyribose-5-phosphate (dRP) moiety via its dRP lyase activity. Through gel electrophoresis and kinetic analysis of partial BER reconstitution, we demonstrated that gap-filling DNA synthesis by the polymerase activity likely occurred after Schiff base formation but before β-elimination, the two chemical reactions catalyzed by the dRP lyase activity. The Schiff base formation and β-elimination intermediates were trapped by sodium borohydride reduction and identified by mass spectrometry and X-ray crystallography. Presteady-state kinetic analysis revealed that cross-linked Polβ (i.e., reduced Schiff base) exhibited a 17-fold higher polymerase efficiency than uncross-linked Polβ. Conventional and time-resolved X-ray crystallography of cross-linked Polβ visualized important intermediates for its dRP lyase and polymerase activities, leading to a modified chemical mechanism for the dRP lyase activity. The observed interlocking enzymatic activities of Polβ allow us to propose an altered mechanism for the BER pathway, at least under the conditions employed. Plausibly, the temporally coordinated activities at the two Polβ active sites may well be the reason why Polβ has both active sites embedded in a single polypeptide chain. This proposed pathway suggests a corrected facet of BER and DNA repair, and may enable alternative chemical strategies for therapeutic intervention, as Polβ dysfunction is a key element common to several disorders.

DNA base excision repair pathway | DNA polymerase β | dRP lyase chemical mechanism | Schiff base formation | β-elimination

One of the major cellular pathways for repair of DNA damage is base excision repair (BER) (1–5). In this pathway (Scheme 1*A*), DNA lesions are removed by glycosylases (e.g., uracil by uracil–DNA glycosylase [UDG]) before the damaged DNA strand is incised by apurinic/apyrimidinic (AP) endonuclease, resulting in a single-nucleotide gap flanked by a 3′-OH and a 5′-deoxyribose-5-phosphate (dRP) moiety. Subsequently, DNA polymerase β (Polβ) is presumed to first catalyze gap-filling DNA synthesis through its DNA polymerase activity and then perform dRP cleavage via its dRP lyase activity, leaving a nicked DNA substrate for ligation by either Ligase III/XRCC1 or Ligase I (6–12).

The dRP lyase active site resides within the 8-kDa N-terminal domain of Polβ, whereas the polymerase active site sits at the palm subdomain (*SI Appendix*, Fig. S1*A*) (7). Previously, Polβ has been shown to remove a dRP moiety through a Schiff base–mediated β-elimination reaction (13) rather than through hydrolysis (7–10, 14, 15). A Schiff base is generated following nucleophilic attack by the side chain of an active site lysine residue on the sugar C1′ atom of the dRP moiety (step 1 in Scheme 2). Whereas biochemical data suggest that K72 in human polymerase-β (hPolβ) acts as the active site nucleophile, conflicting evidence as well as a lack of supporting structural data have complicated understanding of the dRP cleavage mechanism (10, 14, 15). For instance, mutation of K72 to alanine does not fully abrogate the dRP lyase activity, suggesting that a different residue may support the nucleophilic attack on the C1′ (11). Furthermore, only limited conclusions can be drawn from the existing binary crystal structures of hPolβ bound to either a single-nucleotide gapped DNA substrate (hPolβ•DNA^{P}) (*SI Appendix*, Fig. S2*B*) containing only a 5′-phosphate, rather than a full dRP moiety, on the downstream primer (*SI Appendix*, Fig. S2 *A*, *i*) (16) or a nicked DNA substrate (hPolβ•DNA^{THF}) (*SI Appendix*, Fig. S2*C*) containing a 5′-dRP mimic (*SI Appendix*, Fig. S2 *A*, *ii*) (11). Due to the lack of the deoxyribose moiety in the structure of hPolβ•DNA^{P}, information about the dRP cleavage mechanism is lacking. On the other hand, in the structure of hPolβ•DNA^{THF}, the nonnatural dRP mimic was bound in a nonproductive docking site stabilized through the interaction between its 5′-phosphate and K68 (*SI Appendix*, Fig. S2*C*). This nonproductive site is distinct from the putative dRP lyase active site as the Nε atom of K72 is more than 10 Å from the dRP sugar C1′ (11). In fact, from this position, the dRP must rotate ∼120° around the 3′-phosphate to be in close-enough proximity to the Nε atom of K72 for nucleophilic attack to occur (*SI Appendix*, Fig. S2*C*). Furthermore, the active site residues responsible for stabilizing the reactive ring-opened aldehyde state of the dRP moiety and abstracting a proton from the ribose C2′ atom to facilitate β-elimination (Scheme 2) remain unidentified.

Significance

Base excision repair (BER) is one of the major DNA repair pathways used to fix a myriad of cellular DNA lesions. The enzymes involved in BER, including DNA polymerase β (Polβ), have been identified and characterized, but how they act together to efficiently perform BER has not been fully understood. Through gel electrophoresis, mass spectrometry, and kinetic analysis, we discovered that the two enzymatic activities of Polβ can be interlocked, rather than functioning independently from each other, when processing DNA intermediates formed in BER. The finding prompted us to hypothesize a modified BER pathway. Through conventional and time-resolved X-ray crystallography, we solved 11 high-resolution crystal structures of cross-linked Polβ complexes and proposed a detailed chemical mechanism for Polβ's 5′-deoxyribose-5-phosphate lyase activity.

Author contributions: Z.S. designed research; A.K., A.J.R., W.J.Z., and S.M.D. performed research; A.K., A.J.R., W.J.Z., and Z.S. analyzed data; Z.S., A.J.R., and A.K. wrote the paper; and Z.S., S.M.H., A.J.R., S.M.D., W.J.Z., and A.K. edited the manuscript.

The authors declare no competing interest.

This article is a PNAS Direct Submission.

[1]To whom correspondence may be addressed. Email: zucai.suo@med.fsu.edu.

This article contains supporting information online at http://www.pnas.org/lookup/suppl/doi:10.1073/pnas.2118940119/-/DCSupplemental.

Published March 1, 2022.

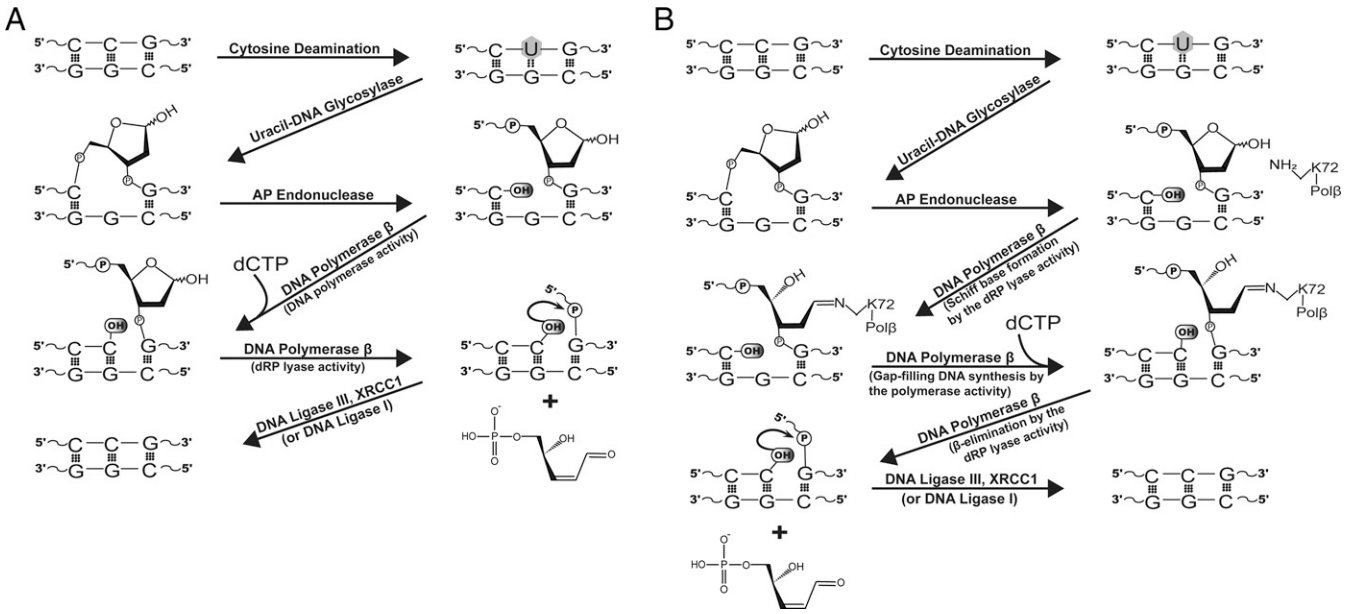

Scheme 1. The BER pathway. (*A*) The BER pathway in the literature as cited in the Introduction. (*B*) Our proposed BER pathway.

Biochemical studies of the processing of dRP moieties in yeast cell-free extract (17), steady-state kinetic studies of fully reconstituted human BER (4), and investigation of the numbers of endogenous AP sites in genomic DNA of rats and human tissue (5) all suggest that dRP cleavage is the rate-limiting step of the entire BER pathway. However, there is no experimental evidence to indicate that all potential steps associated with dRP cleavage by the lyase activity of Polβ (Scheme 2) occur after gap-filling DNA synthesis catalyzed by the polymerase activity. For example, if facile Schiff base formation occurs before and faster than nucleotide incorporation, the covalently linked Polβ–DNA intermediate, rather than the noncovalent binary complex Polβ•DNA, may catalyze gap-filling DNA synthesis. This possibility has never been

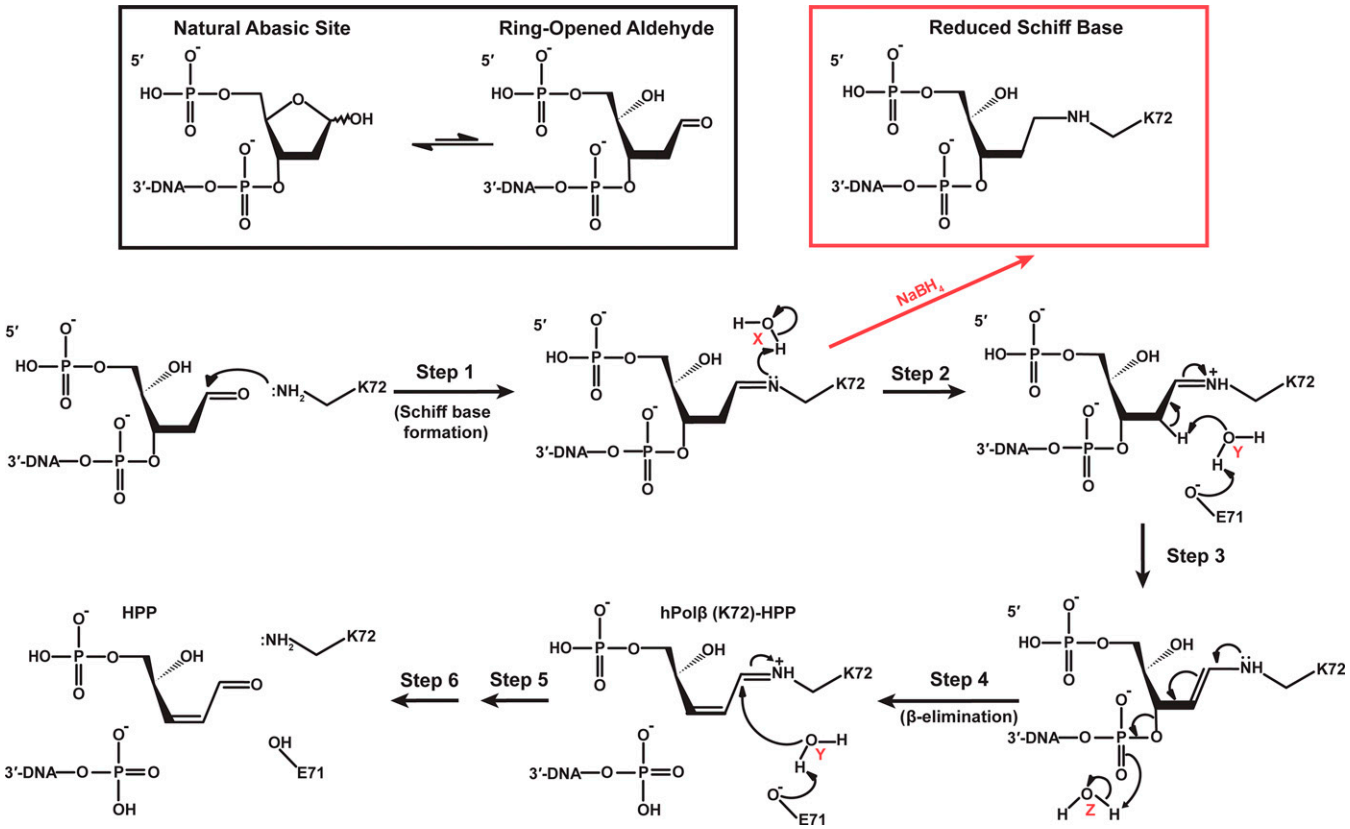

Scheme 2. Proposed chemical mechanism for the dRP lyase activity of hPolβ. Specific water molecules are denoted as X, Y, and Z.

investigated, and all previously published in vitro studies have used DNA substrates like either DNA^{P} (*SI Appendix*, Fig. S2 *A*, *i*) (18–24) or a gapped DNA substrate containing a dRP mimic (*SI Appendix*, Fig. S2 *A*, *ii*) (11, 25).

Here, we generated a natural dRP moiety by using either UDG to process a nicked DNA substrate containing a 2′-deoxyuridine or UDG and apurinic/apyrimidinic endonuclease 1 (APE1) to initiate BER on a double-stranded DNA substrate containing a 2′-deoxyuridine. Addition of hPolβ, correct deoxynucleoside triphosphate (dNTP), and then, sodium borohydride ($NaBH_4$) to the dRP-containing DNA products allowed for the capture of a reduced Schiff base and a β-elimination intermediate produced via hPolβ-catalyzed dRP cleavage (Scheme 2). Through X-ray crystallographic, kinetic, and mass spectrometric (MS) analysis of these cross-linked hPolβ complexes, we envisioned a detailed chemical mechanism for the dRP lyase activity of hPolβ. In addition, we utilized presteady-state kinetic methods to evaluate the impact of the reduced Schiff base intermediate on the efficiency and fidelity of gap-filling DNA synthesis by the polymerase activity of hPolβ. Finally, we employed time-resolved X-ray crystallography to structurally characterize intermediates of gap-filling DNA synthesis by cross-linked hPolβ. Based on several lines of experimental evidence, we proposed a modified BER pathway (Scheme 1*B*), which posits an interlocking mechanism in which gap-filling DNA synthesis by the polymerase activity occurs between Schiff base formation and β-elimination, the two steps catalyzed by the lyase activity.

Results

Investigating the Order of Enzymatic Reactions Catalyzed by hPolβ during BER. To investigate if both Schiff base formation and β-elimination associated with dRP cleavage by the lyase activity of Polβ occur after gap-filling DNA synthesis catalyzed by the polymerase activity of Polβ during BER, we treated a doubly [^{32}P]-labeled and 2′-deoxyuridine–containing nicked DNA substrate $DNA1^{N}$ with UDG to generate a single-nucleotide gapped DNA substrate $DNA1^{dRP}$ containing a freshly produced abasic site (Fig. 1*A*), which was subsequently reduced by $NaBH_4$ (lane C3 in Fig. 1*B*). The conversion of the downstream primer 19-mer to dRP–18-mer was supported by the slightly faster migration of the downstream primer after the treatment of $DNA1^{N}$ with UDG, not with hPolβ (comparing lanes C3 and C2 in Fig. 1*B*). Next, $DNA1^{dRP}$ was mixed with the solution of hPolβ and correct deoxycytidine triphosphate (dCTP) (100 μM) for various times before being quenched by ethylenediaminetetraacetic acid (EDTA) and reduced by $NaBH_4$ (*Materials and Methods*). The reaction mixtures were then analyzed by both urea-based DNA sequencing gel electrophoresis (Fig. 1*B*) and sodium dodecyl sulfate polyacrylamide gel electrophoresis (SDS-PAGE) (Fig. 1*C*). The 13-mer band generated from dCTP incorporation into the upstream primer 12-mer in $DNA1^{dRP}$ initially appeared at 0.064 s, and its intensity increased with time (Fig. 1*B*). Meanwhile, two hPolβ–DNA cross-linked intermediates were formed with their bands detectable as early as 0.032 and 0.256 s (Fig. 1*C*). The first cross-linked intermediate appeared earlier and migrated more slowly, and thus it has a higher molecular weight than the second cross-linked intermediate (Fig. 1*C*). The band intensity for each of the cross-linked intermediates initially increased and then decreased with time, but the first intermediate appeared and peaked earlier (Fig. 1 *C* and *D*), suggesting that the second intermediate was possibly derived from the first one. Similarly, the first cross-linked intermediate probably originated from the downstream primer 19-mer, considering that the band intensity of 19-mer decreased with time, while the band intensity of the first intermediate initially increased with time (Fig. 1 *B*–*D*). To further identify the cross-linked intermediates, the most intense gel bands at 0.256 s (the first cross-linked intermediate) and 20 s (the second cross-linked intermediate) (Fig. 1*C*) were cut for in-gel trypsin digestion and then, MS analysis. The tandem MS/MS analysis (*SI Appendix*, Fig. S3) indicates that the cross-linked intermediate in the 20-s band was formed from the $NaBH_4$ reduction of hPolβ (K72)–*cis*-4-hydroxy-2-pentenal-5-phosphate (HPP; an α,β-unsaturated derivative of dRP), one of the two β-elimination products (step 4 in Scheme 2). However, the cross-linked intermediate in the 0.256s band was difficult to analyze by both MS/MS and matrix assisted laser desorption/ionization-time of flight analysis, likely due to the highly negatively charged DNA oligomer (dRP–18-mer) covalently attached to hPolβ (*SI Appendix*, Fig. S4*A*). To overcome the problem, the cross-linked intermediate was first extracted from the 0.256-s band and then treated with the nucleoside digestion mix (New England Biolabs) in order to shorten the cross-linked dRP–18-mer to the last nucleoside 2'-deoxyguanine (dG) or a smaller fragment (26, 27), followed by the separation on SDS-PAGE and in-gel digestion by trypsin. Through MS/MS analysis of the tryptic products (*SI Appendix*, Fig. S3), we observed various fragment ions of the fragment (*SI Appendix*, Fig. S3 *F*–*H*), including dRP–phosphate (V in *SI Appendix*, Fig. S3*A*) cross-linked to K72 in the peptide (residues 69 to 81 of hPolβ: IAEKIDEFLATGK) as previously reported (14). This suggests that the cross-linked intermediate in the 0.256s band is hPolβ (K72)–dRP–18-mer. This conclusion was further supported by 11 crystal structures (see below) of hPolβ cross-linked to DNA^{dRP} (*SI Appendix*, Fig. S2 *A*, *iii*), a smaller version of $DNA1^{dRP}$ (Fig. 1*A*). The successful identification of hPolβ (K72)–dRP–18-mer confirms that the first cross-linked intermediate was generated through Schiff base formation between 19-mer and hPolβ (step 1 in Scheme 2). Together, the above analysis suggests the series reactions of 19-mer → hPolβ (K72)–dRP–18-mer → hPolβ (K72)–HPP catalyzed by the dRP lyase activity. However, it is difficult to determine the accurate concentrations of these species for three reasons: 1) The $NaBH_4$ reduction only helped to capture portions of the cross-linked intermediates. 2) The cross-linked intermediates were partially degraded by the very basic buffer due to the presence of a large amount of $NaBH_4$ (Fig. 1*C*). 3) It was difficult to separate the uncross-linked 5′-[^{32}P]–19-mer and [^{32}P]-labeled *cis*-4-hydroxy-2-pentenol-5-phosphate (HPP′; the reduced alcohol form of HPP) from other species in free probes (Fig. 1*C*). Accordingly, we estimated the concentrations of these species (*SI Appendix*) and then, estimated the 5′-[^{32}P]–19-mer consumption rate ($4 \pm 1\ s^{-1}$), the Schiff base formation rate ($4.5 \pm 0.4\ s^{-1}$), and the β-elimination rate ($0.31 \pm 0.05\ s^{-1}$) through the early reaction time points (Fig. 1 *E*, *F*, and *H*). Interestingly, the rates for 5′-[^{32}P]–19-mer consumption and Schiff base formation are comparable, and this seems reasonable because the Schiff base was formed from 19-mer (see above). In comparison, dCTP at its in vivo concentration (100 μM) was incorporated at a rate of $0.8 \pm 0.3\ s^{-1}$ (Fig. 1*G*). Thus, Schiff base formation ($4.5\ s^{-1}$) was determined to be 5.6-fold faster than polymerase-catalyzed gap-filling DNA synthesis ($0.8\ s^{-1}$), which was found to be 2.6-fold faster than β-elimination ($0.31\ s^{-1}$). The rate order was consistent with the initial appearance times of hPolβ (K72)–[^{32}P]–dRP–18-mer (0.032 s), [^{32}P]–13-mer (0.064 s), and hPolβ (K72)–[^{32}P]–HPP (0.256 s) (Fig. 1 *B* and *C*). Together, these results suggested that hPolβ catalyzes Schiff base formation prior to the gap-filling DNA synthesis followed by β-elimination during BER.

Furthermore, we investigated if the dRP lyase-catalyzed reactions were coupled with the polymerase-catalyzed dNTP incorporation during BER by performing the same assay in Fig. 1 but either in the presence of 1 μM dCTP or in the absence of any dNTPs (*SI Appendix*, Fig. S4). With 1 μM dCTP, the initial appearance times for hPolβ (K72)–[^{32}P]–dRP–18-mer, [^{32}P]–13-mer, and hPolβ (K72)–[^{32}P]–HPP were 0.032, 0.064, and 0.256 s, respectively (*SI Appendix*, Fig. S4 *H*–*J*),

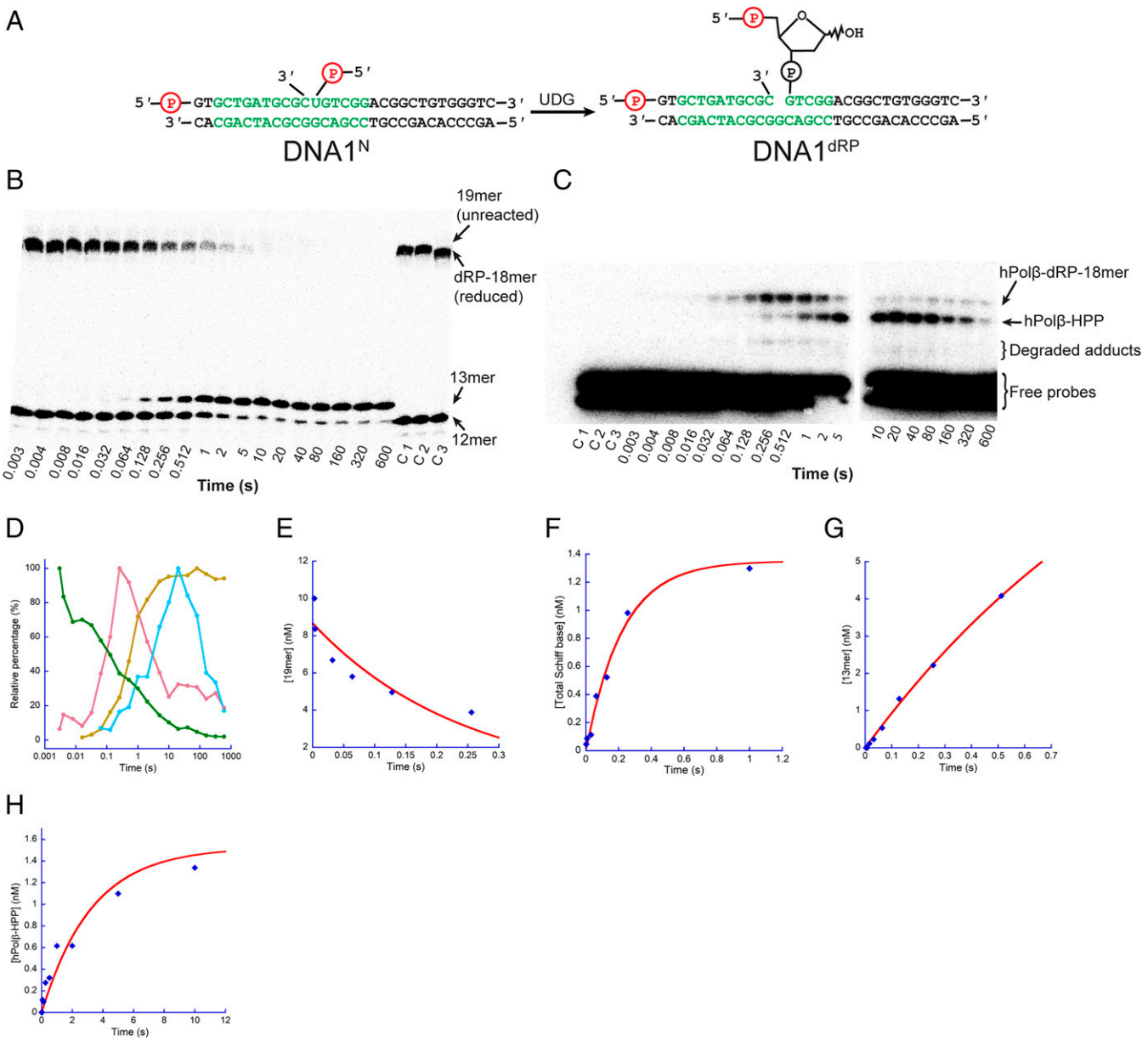

Fig. 1. Two hPolβ–DNA cross-linked intermediates formed during gap-filling DNA synthesis. DNA1^{N} (10 nM) was processed by UDG to form DNA1^{dRP} containing dRP–18-mer (*A*). Each circled "P" denotes a ^{32}P-labeled phosphate, while the identical base sequences in DNA1^{dRP} and DNA^{dRP} (*SI Appendix*, Fig. S2 *A*, *iii*) are shown in green. The newly formed 5′-[^{32}P]–DNA1^{dRP} was mixed with hPolβ (200 nM) and dCTP (100 μM) to form both cross-linked hPolβ–DNA complexes and 13-mer at different time intervals (*Materials and Methods*). After $NaBH_4$ reduction and trapping, equal volumes of the reaction mixtures were loaded and analyzed by both urea-based PAGE (*B*) and SDS-PAGE (*C*). In *B*, lanes C1, C2, and C3 denote 5′-[^{32}P]–DNA1^{N} after the $NaBH_4$ reduction treatment, 5′-[^{32}P]–DNA1^{N} after being treated with UDG and then $NaBH_4$ reduction, and 5′-[^{32}P]–DNA1^{N} after being treated with hPolβ and then $NaBH_4$ reduction, respectively. In *C*, free probes represent [^{32}P]-labeled species (19-mer, reduced dRP–18-mer, 13-mer, 12-mer, and HPP′). The percentages of the band intensities of [^{32}P]–19-mer (green), hPolβ (K72)–[^{32}P]–dRP–18-mer (salmon), [^{32}P]–13-mer (gold), and hPolβ (K72)–[^{32}P]–HPP (blue) relative to the intensities of their corresponding most-intense bands were individually plotted against time in a semilog fashion (*D*). The concentrations of [^{32}P]–19-mer, total Schiff base formation products (hPolβ (K72)–[^{32}P]–dRP–18-mer and hPolβ (K72)–[^{32}P]–HPP), [^{32}P]–13-mer, and hPolβ (K72)–[^{32}P]–HPP are plotted against time from their early reaction time points in *E*–*H*, respectively. The plots were fit to [product] = $A\exp(-k_{obs}t)$ to obtain the observed 19-mer consumption rate k_{obs} (4 ± 1 s^{-1}; *E*), or [product] = $A[1 - \exp(-k_{obs}t)]$ to yield theobserved rate k_{obs} for gap-filling DNA synthesis (0.8 ± 0.3 s^{-1}; *G*), Schiff base formation (4.5 ± 0.4 s^{-1}; *F*), or β-elimination (0.31 ± 0.05 s^{-1}; *H*). *A* indicates the reaction amplitude.

while the rates of Schiff base formation, gap-filling DNA synthesis, and β-elimination were estimated to be 4.9 ± 0.9, 0.35 ± 0.04, and 0.20 ± 0.05 s^{-1}, respectively (*SI Appendix*, Fig. S4 *L–N*). The 5′-[^{32}P]–19-mer consumption rate was also estimated to be 3 ± 2 s^{-1} (*SI Appendix*, Fig. S4*K*). All of those values are either the same or comparable with those corresponding values with 100 μM dCTP except the 2.3-fold-lower dCTP incorporation rate, which was due to the 100-fold-lower dCTP concentration. These data further suggest that the pattern of Schiff base formation prior to gap-filling DNA synthesis followed by β-elimination during BER was not altered by the change in dCTP concentration. Similarly, in the absence of dNTPs, the bands of hPolβ (K72)–[^{32}P]–dRP–18-mer and hPolβ (K72)–[^{32}P]–HPP initially appeared at 0.032 and 0.256 s, respectively (*SI Appendix*, Fig. S4 *A–D*), while Schiff base formation and β-elimination occurred at rates of 6 ± 1 and

0.49 ± 0.04 s^{-1}, respectively (*SI Appendix*, Fig. S4 *F* and *G*). In the meantime, the upstream primer 12-mer was not elongated at all (*SI Appendix*, Fig. S4*B*), while the downstream primer 19-mer was consumed at a rate of 4.5 ± 0.8 s^{-1} (*SI Appendix*, Fig. S4*E*). Considering that these kinetic data were comparable with those corresponding values obtained with either 100 or 1 μM dCTP (*SI Appendix*, Fig. S4*O*), we suggest that the dRP lyase activity of hPolβ acts similarly in the presence or absence of a correct dNTP and is thus independent of the polymerase activity. However, the polymerase activity may be impacted by rapid and preceding Schiff base formation catalyzed by the dRP lyase activity. This possibility was kinetically investigated.

Nucleotide Incorporation Efficiency and Fidelity with the Cross-Linked hPolβ (K72)–DNA^{dRP} Complex. While the kinetic and structural mechanisms of DNA synthesis catalyzed by uncross-linked hPolβ have been extensively studied with model DNA substrates like DNA^{P} (*SI Appendix*, Fig. S2 *A*, *i*) (24, 28–31), the effect of a natural dRP (*SI Appendix*, Fig. S2 *A*, *iii*) and a Schiff base intermediate (step 1 in Scheme 2) on the kinetics of nucleotide incorporation and the polymerase active site structure has yet to be investigated. To fill this void, we performed another partial BER reconstitution by treating a 2′-deoxyuridine–containing double-stranded DNA substrate with UDG, APE1, and hPolβ followed by quenching and $NaBH_4$ reduction (additional methods are in *SI Appendix*). After purification, the cross-linked and reduced hPolβ–DNA^{dRP} complex was used to determine the kinetic effect of the Schiff base intermediate (Scheme 2) on gap-filling DNA synthesis. For comparison, we performed presteady-state kinetic assays to determine kinetic parameters for correct or incorrect dNTP incorporation onto either 5′-[^{32}P]–DNA^{dRP} (*SI Appendix*, Fig. S2 *A*, *iii*) cross-linked to hPolβ (K72) or 5′-[^{32}P]–DNA^{P} (*SI Appendix*, Fig. S2 *A*, *i*) uncross-linked to hPolβ (Table 1 and *SI Appendix*, Fig. S5). Notably, DNA^{dRP}, a shorter version of DNA1^{dRP} (Fig. 1*A*), has the identical base sequences as DNA^{P}. The kinetic results of correct dCTP incorporation onto the hPolβ–[^{32}P]–DNA^{dRP} were further confirmed through assays with α-[^{32}P]–dCTP and unlabeled hPolβ–DNA^{dRP} (*SI Appendix*, Fig. S5 *I* and *R*). The maximal correct dCTP incorporation rate (k_p) for hPolβ–DNA^{dRP} (0.72 s^{-1}) was expected to be close to the above estimated rate of 0.8 s^{-1} (Fig. 1*G*) under the saturating dCTP concentration (100 μM vs. K_d of 0.38 μM in Table 1) but was fourfold lower than the k_p with uncross-linked hPolβ•DNA^{P} (2.9 s^{-1}), suggesting that the cross-link slowed dCTP incorporation. Although maximal misincorporation rates varied for the cross-linked and uncross-linked hPolβ complexes, misincorporation was uniformly slower than correct incorporation (Table 1). Interestingly, the apparent binding affinity ($1/K_d$) for correct dCTP was increased by 68-fold for cross-linked (K_d = 0.38 μM) relative to uncross-linked hPolβ (K_d = 26 μM). Similarly, the cross-link also increased the affinity for incorrect dNTPs by three- to ninefold (Table 1). To confirm the tight binding affinity of correct dCTP, we performed microscale thermophoresis assays (32) with cross-linked hPolβ–DNA^{dRP} and increasing concentrations of dCTP, which yielded a comparable K_d value of 0.5 ± 0.2 μM for dCTP binding (*SI Appendix*, Fig. S5*S*). Strikingly, the polymerase efficiency (k_p/K_d) of dCTP incorporation was increased by 17-fold due to the cross-link (Table 1). Importantly, the 17-fold enhancement in the gap-filling DNA synthesis efficiency for hPolβ–DNA^{dRP} relative to hPolβ•DNA^{P} resulted in an insignificant change of polymerase fidelity (10^{-5} to 10^{-6}) (Table 1). Together, these kinetic data indicated that preceding Schiff base formation significantly enhances the gap-filling polymerase activity of hPolβ in the system that we employed.

Binary Crystal Structures of hPolβ Cross-Linked with DNA via a Natural dRP Moiety. To gain structural insight into the dRP cleavage mechanism, the above cross-linked and reduced hPolβ–DNA^{dRP} complex was crystallized, and two structures, (hPolβ–DNA^{dRP})$_A$ and (hPolβ–DNA^{dRP})$_B$, were solved at 1.89- and 1.84-Å resolution, respectively, through molecular replacement (Fig. 2 and *SI Appendix*, Fig. S1 *A* and *B* and Table S1). Notably, both hPolβ–DNA^{dRP} structures display clear electron density for the reduced dRP in the ring-opened form and cross-linked to K72 (Fig. 2 *A* and *B*). These structures firmly corroborate the Schiff base formation product hPolβ (K72)–dRP–18-mer as inferred from the above MS/MS analysis. Both (hPolβ–DNA^{dRP})$_A$ and (hPolβ–DNA^{dRP})$_B$ superimposed well with each other (rmsd of 0.40 Å) (*SI Appendix*, Fig. S1*E*) and with the uncross-linked hPolβ•DNA^{P} (rmsds of 0.63 and 0.73 Å, respectively) (16) and hPolβ•DNA^{THF} (rmsds of 0.67 and 0.74 Å, respectively) (11) structures, confirming that the cross-link did not adversely affect the overall protein structure (*SI Appendix*, Fig. S1*E*). Interestingly, (hPolβ–DNA^{dRP})$_A$ and (hPolβ–DNA^{dRP})$_B$ exhibit different binding conformations of the cross-linked and reduced dRP moiety (Fig. 2*C*). This suggested that the dRP remains mobile in the dRP lyase active site despite being covalently attached to hPolβ. In contrast, the uncross-linked hPolβ•DNA^{THF} showed that the dRP-mimic moiety (*SI Appendix*, Fig. S2 *A*, *ii*) is bound at a single nonproductive docking site within the dRP lyase active site that would require ∼120° rotation about the C5′-O-3′-phosphate bond for Schiff base formation (*SI Appendix*, Fig. S2*C*) (11).

The dRP lyase active site of (hPolβ–DNA^{dRP})$_B$ superimposed well with those of uncross-linked hPolβ•DNA^{P} and hPolβ•DNA^{THF} (*SI Appendix*, Fig. S2*D*). For example, the side chain of K35 was observed in the same position in all structures and likely functions to anchor the downstream primer to the active site through its interaction with the 3′-phosphate covalently connected to the dRP in the downstream primer (*SI Appendix*, Fig. S2 *C–F*). K72 was also observed in similar

Table 1. Kinetic parameters for gap-filling DNA synthesis catalyzed by cross-linked or uncross-linked hPolβ at 25 °C

Nucleotide	k_p (s^{-1})	K_d (μM)	k_p/K_d ($\mu M^{-1}s^{-1}$)	Fidelity*
Cross-linked hPolβ–DNA^{dRP} complex (DNA^{dRP}, see *SI Appendix*, Fig. S2 *A*, *iii*).				
dCTP	0.72 ± 0.05	0.38 ± 0.08	1.9	—
dATP	$(4.5 \pm 0.2) \times 10^{-3}$	56 ± 10	8.0×10^{-5}	4.2×10^{-5}
dGTP	$(5.7 \pm 0.1) \times 10^{-4}$	166 ± 12	3.4×10^{-6}	1.8×10^{-6}
dTTP	0.020 ± 0.001	169 ± 34	1.2×10^{-4}	6.3×10^{-5}
Uncross-linked hPolβ and DNA^{P} (*SI Appendix*, Fig. S2 *A*, *i*)				
dCTP	2.9 ± 0.2	26 ± 4	0.11	—
dATP	$(1.0 \pm 0.2) \times 10^{-3}$	510 ± 267	2.0×10^{-6}	1.8×10^{-5}
dGTP	$(3.7 \pm 0.6) \times 10^{-3}$	494 ± 171	7.5×10^{-6}	6.8×10^{-5}
dTTP	$(1.0 \pm 0.1) \times 10^{-3}$	858 ± 274	1.2×10^{-6}	1.1×10^{-5}

dATP, 2′-deoxyadenosine 5′-triphosphate; dGTP, 2′-deoxyguanosine 5′-triphosphate; dTTP, 2′-deoxythymidine 5′-triphosphate.
*Defined as $(k_p/K_d)_{incorrect}/[(k_p/K_d)_{incorrect} + (k_p/K_d)_{correct}]$.

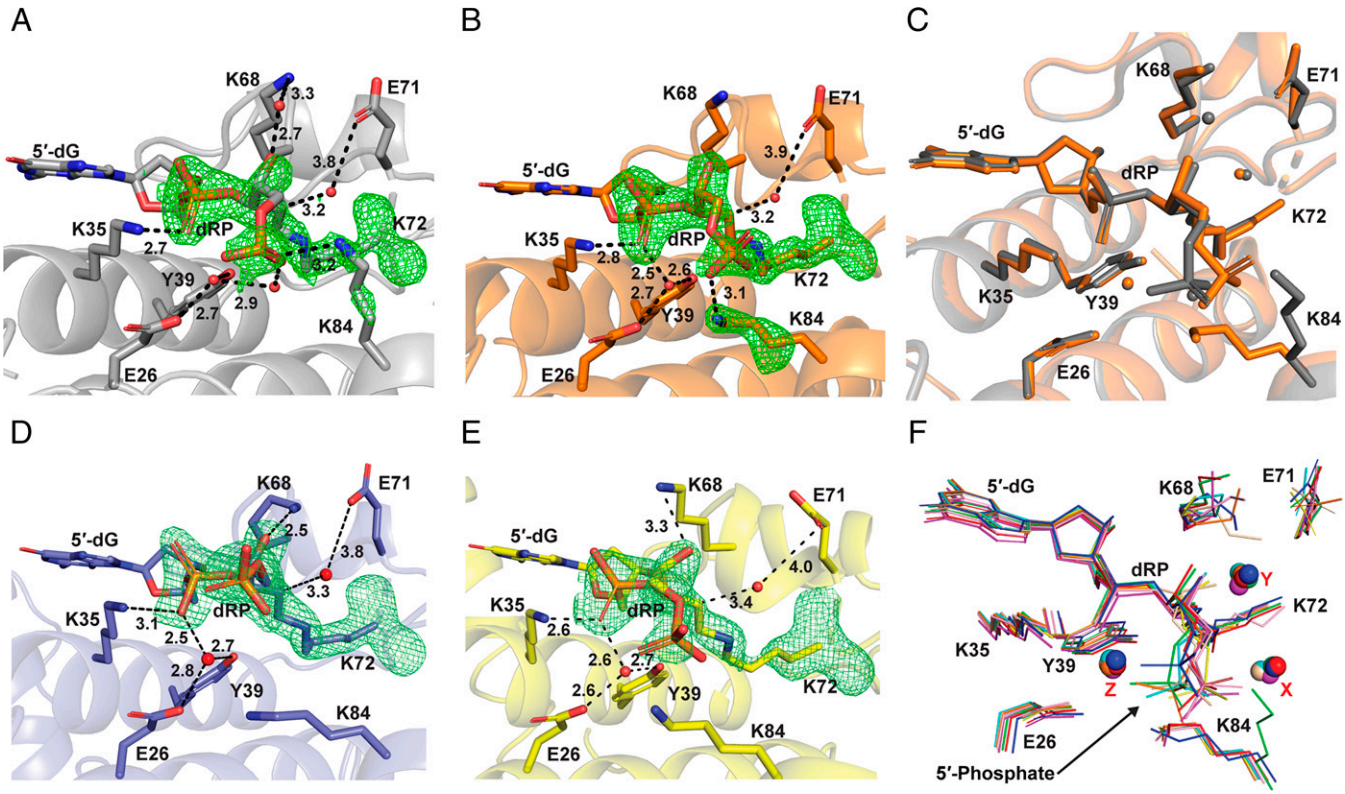

Fig. 2. hPolβ dRP lyase active site comparison. (*A* and *B*) dRP lyase active sites of the (hPolβ–DNA^{dRP})$_A$ (*A*; gray) and (hPolβ–DNA^{dRP})$_B$ (*B*; orange) complexes. (*C*) Superposition of (hPolβ–DNA^{dRP})$_A$ (gray) and (hPolβ–DNA^{dRP})$_B$ (orange). Water molecules are depicted as spheres in the respective colors of the overlapped complexes. (*D* and *E*) dRP lyase active sites of the (hPolβ–DNA^{dRP}•dNTP)$_1$ (*D*; blue) and (hPolβ–DNA^{dRP}•dNTP)$_2$ (*E*; yellow) complexes. In *A*, *B*, *D*, and *E*, water molecules are depicted as red spheres. (*F*) Overlay of dRP lyase active sites in (hPolβ–DNA^{dRP})$_A$ (green), (hPolβ–DNA^{dRP})$_B$ (red), (hPolβ–DNA^{dRP}•dNTP)$_1$ (blue), and (hPolβ–DNA^{dRP}•dNTP)$_2$ (yellow) for 20 s (magenta), 30 s (cyan), 40 s (orange), 60 s (wheat), 20 min (gray), and 60 min (black) of Ca^{2+} to Mg^{2+} exchange and 60 s of Ca^{2+} to Mn^{2+} exchange (pink). Water molecules X, Y, and Z are shown as spheres colored as in their corresponding structures. Electron densities F_o–F_c omit maps (green; 3σ) are shown for the cross-linked and ring-opened dRP moiety as well as K84 in *A* and *B*. Important interactions are shown as dashed lines with distances in angstroms.

positions among the binary structures, suggesting that dRP repositioning, rather than a protein conformational change, placed the dRP moiety for cleavage in the dRP lyase active site (*SI Appendix*, Fig. S2*D*). Interestingly, the K84 residue of the (hPolβ–DNA^{dRP})$_A$ and (hPolβ–DNA^{dRP})$_B$ structures exhibited different rotameric configurations with K84 of (hPolβ–DNA^{dRP})$_B$ (Fig. 2*B*) adopting a similar position as in hPolβ•DNA^P and hPolβ•DNA^{THF} (*SI Appendix*, Fig. S2*D*). The alternative conformation of K84 in the (hPolβ–DNA^{dRP})$_A$ structure was accompanied by a slight repositioning (1.5 Å) of the 5′-phosphate of the dRP relative to (hPolβ–DNA^{dRP})$_B$ (Fig. 2*C*). Moreover, in both structures, K84 interacted with the 5′-phosphate of the dRP through charge–charge interactions and likely acts to capture and stabilize the dRP after it rotates into the dRP lyase active site (Fig. 2 *C* and *F*).

Precatalytic Ternary Structures of hPolβ Cross-Linked with DNA in the Presence of a Correct Nucleotide and Noncatalytic Divalent Metal Ions. To provide a structural basis for significantly higher dCTP binding affinity and incorporation efficiency with cross-linked over uncross-linked hPolβ (Table 1), we crystalized and determined two ternary structures of hPolβ–DNA^{dRP}•dCTP [(hPolβ–DNA^{dRP}•dNTP)$_1$ and (hPolβ–DNA^{dRP}•dNTP)$_2$] in the presence of noncatalytic Ca^{2+}, rather than catalytic Mg^{2+} (*SI Appendix*, Fig. S1 *C* and *D* and Table S1). Both (hPolβ–DNA^{dRP}•dNTP)$_1$ and (hPolβ–DNA^{dRP}•dNTP)$_2$ superimpose well with the uncross-linked ternary structure of hPolβ•DNA^P•dCTP with Ca^{2+} (18), with rmsd values of 0.806 and 0.763 Å, respectively (*SI Appendix*, Fig. S1*F*). Relative to the hPolβ–DNA^{dRP} binary structures, both (hPolβ–DNA^{dRP}•dNTP)$_1$ and (hPolβ–DNA^{dRP}•dNTP)$_2$ contained a closed protein conformation with the typical thumb subdomain closure (*SI Appendix*, Fig. S1*G*) induced by nucleotide binding (33). Notably, the hPolβ conformational closure did not significantly alter the dRP lyase domain structure (*SI Appendix*, Fig. S1*G*) as the cross-linked dRP moiety has well defined electron density (Fig. 2 *D* and *E*) and was observed in a similar position as within the hPolβ–DNA^{dRP} binary structures, except for the relatively free movement of the 5′-phosphate of the dRP moiety (Fig. 2*F*). For instance, water molecule Y that bridges E71 and the C2′ atom of the dRP was in a nearly identical position in the binary and ternary structures (Fig. 2*F*). However, K84 in the hPolβ–DNA^{dRP}•dCTP structures aligns well with the same residue in (hPolβ–DNA^{dRP})$_B$, not in (hPolβ–DNA^{dRP})$_A$ (Fig. 2*F*).

Comparison of the polymerase active site in the hPolβ–DNA^{dRP}•dCTP structures and in hPolβ•DNA^P•dCTP revealed minor positioning changes of active site residues, dCTP, and metal ions (Fig. 3 *A*–*D*). For example, several hydrogen bonds between the side chains of active site residues and the bound dCTP were reduced by 0.1 to 0.3 Å, while the hydrogen bonds in the nascent base pair were shortened by 0.3 to 0.5 Å due to dCTP movement toward the templating dG in the hPolβ–DNA^{dRP}•dCTP structures (Fig. 3 *A*–*C*). Notably, the two 3′-terminal nucleotides of the upstream primer in (hPolβ–DNA^{dRP}•dNTP)$_1$ displayed C1′-exo rather than C3′-endo sugar puckering as observed for the nucleotides in the analogous positions in (hPolβ–DNA^{dRP}•dNTP)$_2$ and hPolβ•DNA^P•dCTP (16, 18, 20, 23). Such an altered sugar puckering in

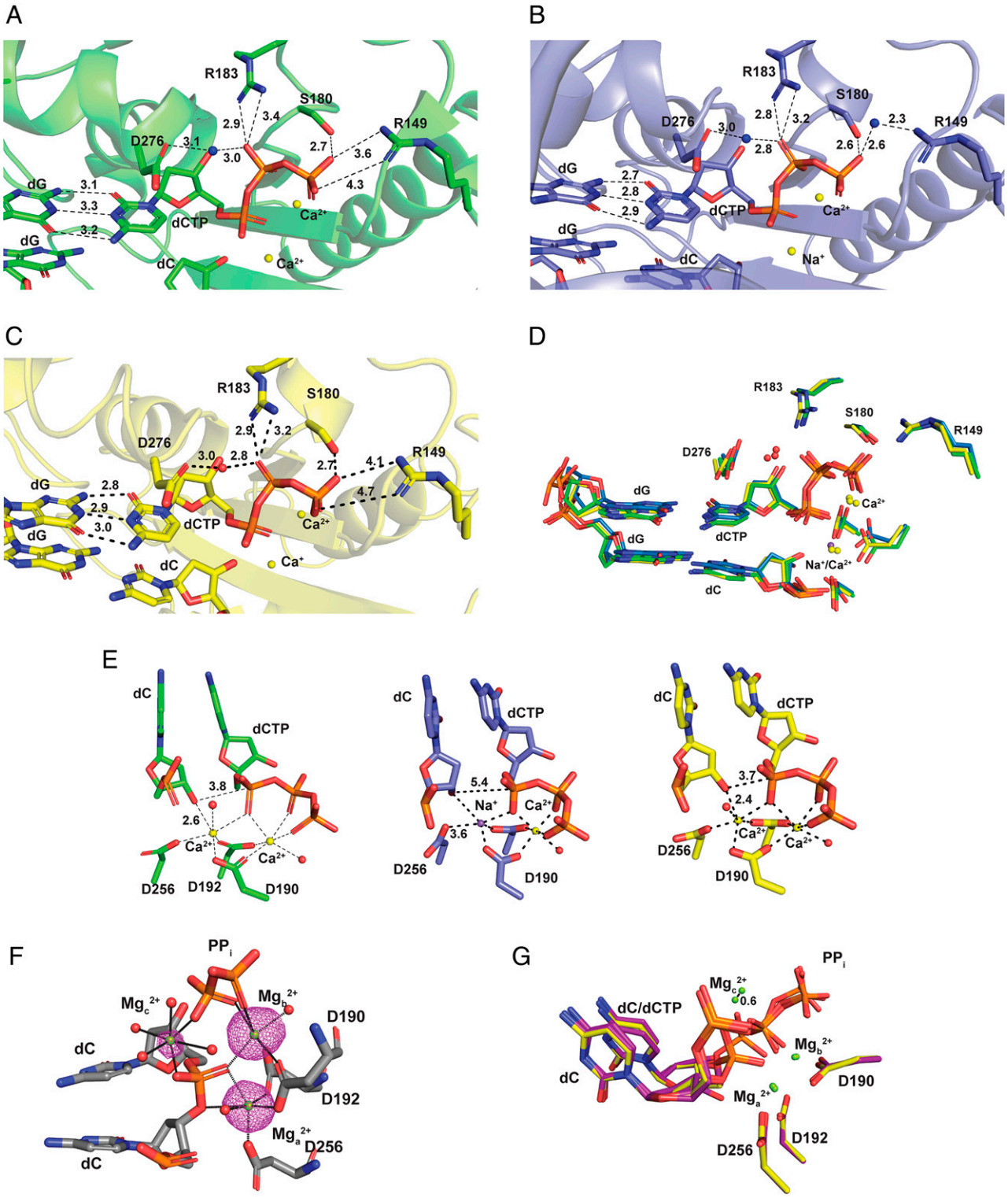

Fig. 3. Comparison of the hPolβ polymerase active site in various structures. (*A*–*C*) Interactions between polymerase active site residues and dCTP are shown for (*A*) hPolβ•DNA^{P}•dNTP (green; Protein Data Bank [PDB] ID code 4KLD), (*B*) (hPolβ–DNA^{dRP}•dNTP)$_1$ (blue), and (*C*) (hPolβ–DNA^{dRP}•dNTP)$_2$ (yellow). (*D*) Superposition of the zoomed polymerase active sites in hPolβ•DNA^{P}•dNTP (green), (hPolβ–DNA^{dRP}•dNTP)$_1$ (blue), and (hPolβ–DNA^{dRP}•dNTP)$_2$ (yellow). Water molecules are shown as red spheres. Calcium and sodium ions are displayed as yellow and purple spheres, respectively. (*E*) Zoomed views of the upstream primer 3′-OH, dCTP, selected active site residues, and metal ions in hPolβ•DNA^{P}•dNTP (green; PDB ID code 4KLD), (hPolβ–DNA^{dRP}•dNTP)$_1$ (blue), and (hPolβ–DNA^{dRP}•dNTP)$_2$ (yellow). (*F*) Zoomed active site showing the primer 3′-terminal deoxycytidine (dC), the incorporated dC, pyrophosphate, aspartate residues, and divalent metal ions after 60 s of Ca^{2+} to Mg^{2+} exchange in crystallo. The metal ion binding sites A, B, and C are designated using a, b, and c, respectively. The electron density (purple; 5σ) depicts the F_o–F_c omit maps for each Mg^{2+} ion. The water molecules are displayed as red spheres. The Mg^{2+} ions are shown as green spheres. (*G*) Overlap of the polymerase active sites in the 40 s (purple) and 60 s (yellow) of Ca^{2+} to Mg^{2+} exchange structures. Each Mg^{2+} is shown as a green sphere. Mg^{2+} at the C site moved by at least 0.6 Å. Important interactions in all panels are shown as dashed lines with distances in angstroms.

(hPolβ–DNA^{dRP}•dNTP)$_1$ caused the upstream primer 3′-OH to flip away from the α-phosphate (Pα) of dCTP and increased the distance between them by 1.7 Å (Fig. 3*E*). Interestingly, the flipped 3′-OH cannot serve as a coordination ligand, resulting in Na^+ bound at the divalent metal ion binding A site in (hPolβ–DNA^{dRP}•dNTP)$_1$ rather than Ca^{2+} as in the (hPolβ–DNA^{dRP}•dNTP)$_2$ and hPolβ•DNA^P•dCTP structures (Fig. 3*E*). The A site in (hPolβ–DNA^{dRP}•dNTP)$_1$ also lacks a coordinating water molecule, which is present in both (hPolβ–DNA^{dRP}•dNTP)$_2$ and hPolβ•DNA^P•dCTP (Fig. 3*E*). As in hPolβ•DNA^P•dCTP, the divalent metal ion binding B site was occupied by Ca^{2+} in both (hPolβ–DNA^{dRP}•dNTP)$_1$ and (hPolβ–DNA^{dRP}•dNTP)$_2$ (Fig. 3*E*).

Snapshots of Nucleotide Incorporation by the Cross-Linked hPolβ–DNA^{dRP} Complex. To investigate if cross-linked hPolβ, like uncross-linked hPolβ (18, 20, 23), can incorporate a correct dNTP in crystallo, we performed Ca^{2+} to Mg^{2+} exchange for 20, 30, 40, and 60 s before flash freezing the crystals in liquid nitrogen (*SI Appendix*). The crystals diffracted to 1.91 to 2.20 Å for the dCTP incorporation intermediates (*SI Appendix*, Table S1), and the structures were solved by molecular replacement (Fig. 4).

For 20, 30, and 40 s of Ca^{2+} to Mg^{2+} exchange (corresponding to 30, 50, and 70% of dCTP incorporation, respectively), partial occupancies of the reactants (the upstream primer 3′-nucleotide and dCTP) and products (pyrophosphate and 2'-deoxycytidine-5'-monophosphate [dCMP]) were modeled to account for the simultaneous electron density gain caused by phosphodiester bond formation between the primer 3′-OH and the Pα of dCTP and loss due to bond breakage between the Pα and β-phosphate of the dCTP (Fig. 4 *A*, *c*–*e*). These features along with the steric inversion of the Pα geometry are consistent with an S_N2 reaction (18, 23, 34). Overall, the time-resolved reaction-state structures are almost superimposable, contain a closed protein conformation, and possess similar dRP lyase and polymerase active sites (Fig. 4 and *SI Appendix*, Fig. S6 *A*, *C*, and *E*). Strikingly, in addition to the two canonical hexacoordinated Mg^{2+} ions at the A site and B site observed in the precatalytic ternary structures (Fig. 3*E*), a third Mg^{2+} at the C site was captured in later reaction stages with an occupancy of 0.7 and 1.0 in structures with 70 and 100% product formation, respectively (Figs. 3*F* and 4 *A*, *e* and *f*). This is similar to previously reported time-resolved structures for dNTP incorporation onto DNA by uncross-linked hPolβ, where ongoing product formation and the appearance of the C-site Mg^{2+} were concurrent events (18, 20–23, 35). From 70 to 100% dCTP incorporation, the C-site Mg^{2+}, coordinated by water molecules and the nonbridging oxygen atoms of Pα and Pβ of dCTP (or nonbridging oxygen atoms of the newly formed phosphodiester bond and pyrophosphate) (Fig. 3*F*), moved 0.6 Å, while the Mg^{2+} ions at the A and B sites did not change their positions (Fig. 3*G*).

To provide additional evidence for the presence of the C-site metal ion, the precatalytic crystals of hPolβ–DNA^{dRP}•dCTP with Ca^{2+} were soaked with Mn^{2+} for 60 s (*SI Appendix*). Like Mg^{2+}, Mn^{2+} supported dCTP incorporation by hPolβ–DNA^{dRP} (*SI Appendix*, Fig. S6*G*). In the resulting 2.21-Å structure (*SI Appendix*, Table S1), the F_o–F_c electron density maps clearly show 100% product formation, two hexacoordinated Mn^{2+} at the A and B sites, and one Mn^{2+} at the C site (Fig. 4 *A*, *i* and *SI Appendix*, Fig. S6*H*). The C-site Mn^{2+} is coordinated by three water molecules and nonbridging oxygen atoms of the newly formed phosphodiester bond and pyrophosphate (*SI Appendix*, Fig. S6*H*). Additionally, overlaying the 60 s of Ca^{2+} to Mg^{2+} exchange and the 60 s of Ca^{2+} to Mn^{2+} exchange product-state structures shows that the three divalent metal ions at each site were nearly superimposable (*SI Appendix*, Fig. S6*I*).

Postcatalytic Binary Structures of hPolβ Cross-Linked with a Nicked DNA Product. After 60 s of Ca^{2+} to Mg^{2+} exchange, the in crystallo reaction was 100% complete, although hPolβ was still in the closed conformation with pyrophosphate bound (Fig. 4 *A*, *f*). To examine if the cross-linked hPolβ can open its conformation after phosphodiester bond formation in order to release pyrophosphate, we performed the Ca^{2+} to Mg^{2+} exchange for 20 and 60 min, and their crystal structures were also solved with resolutions of 2.90 and 2.96 Å, respectively (Fig. 4 *A*, *g* and *h* and *SI Appendix*, Table S1). Interestingly, the cross-linked hPolβ, like uncross-linked hPolβ (18, 20, 23), opened its protein conformation as indicated by the movement of helix N away from the newly incorporated dCMP, the repositioning of active site residues (Y271, F272, D192, D190, and D256), and release of both pyrophosphate and three Mg^{2+} ions (Fig. 4 *A*, *g* and *h*). Surprisingly, the incorporated dCMP in both the 20- and 60-min structures had poor electron density and projected freely rather than base paired with the templating nucleotide dG. The dynamic motion of the incorporated dCMP suggests that the cross-linked hPolβ–nicked DNA product complex is not suitable for further DNA synthesis, therefore requiring β-elimination to occur to complete dRP cleavage and finish the role of hPolβ in BER.

Discussion

Defining a Modified DNA BER Pathway. Previous biochemical, biological, and partial and full in vitro reconstitution studies have determined the sequential reactions catalyzed by four enzymes during BER (4, 5, 17) but assumed that all catalytic actions by the dRP lyase activity of Polβ occur after gap-filling DNA synthesis catalyzed by its polymerase activity (Scheme 1*A*) (4, 12). To investigate whether the two enzymatic activities of hPolβ actually are coupled during BER, the nicked DNA substrate DNA1^N containing a 2′-deoxyuridine was first treated with UDG to form a natural dRP in DNA1^{dRP} (Fig. 1*A*), and the reaction mixture was subsequently mixed with hPolβ and dCTP to initiate the reactions catalyzed by the third BER enzyme. To isolate and identify any unstable cross-linked hPolβ–DNA intermediates formed in the reactions, we used the $NaBH_4$ reduction and trapping approach, which has been previously employed for biochemical and structural characterization of DNA glycosylases (36, 37). Notably, APE1 was not included in our first partial BER reconstitution assay (*Materials and Methods*) because it, like Polβ, can cross-link with a natural abasic site to form a similarly sized protein–DNA cross-linked product (38, 39) and complicate our investigation. As expected, hPolβ incorporated dCTP and extended the upstream primer 12-mer into 13-mer in a time-dependent manner (Fig. 1*B*). In the meantime, the downstream primer 19-mer was gradually consumed, leading to the formation of two hPolβ–DNA cross-linked intermediates (Fig. 1 *B*–*D*). Our MS/MS analysis (*SI Appendix*, Fig. S3) and 11 solved crystal structures (Fig. 4*B*) collectively and consistently identified the cross-linked intermediates as hPolβ (K72)–dRP–18-mer and hPolβ (K72)–HPP. Notably, this is the first time that K72 was structurally identified as the primary nucleophile for Schiff base formation, and the unstable β-elimination intermediate was isolated and identified. Based on the initial appearance times for hPolβ (K72)–dRP–18-mer (0.032s), 13-mer (0.064 s), and hPolβ (K72)–HPP (0.256 s) in the gels (Fig. 1 *B* and *C*) and their initial formation rates of 4.5, 0.8, and 0.31 s^{-1}, respectively, in the presence of 100 μM dCTP (*SI Appendix*, Fig. S4*O*), we propose that Schiff base formation with K72 of hPolβ occurred first followed by gap-filling DNA synthesis and finally, cleavage of the dRP moiety through β-elimination during BER. The reaction order of hPolβ was not affected by dCTP concentration considering that the same initial product appearance times in the gels and comparable k_{obs} values were determined under 1 and 100 μM dCTP (*SI Appendix*, Fig. S4*O*). Taken together, we propose a

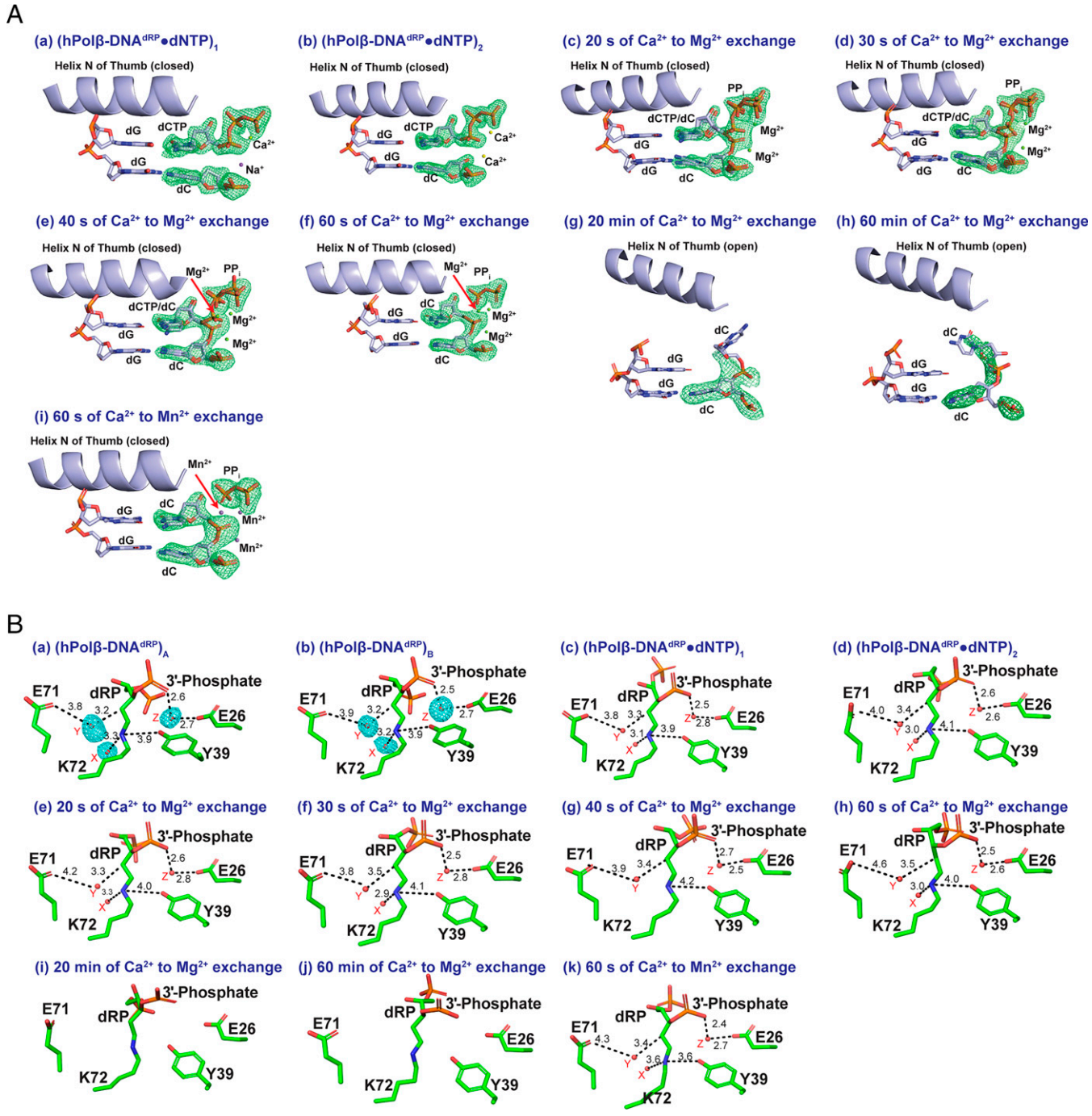

Fig. 4. Time-resolved snapshots of phosphodiester bond formation at the polymerase active site and locations of reactive water molecules at the dRP lyase active site. (*A*) Electron density F_o–F_c omit maps (green; 3σ) are shown for the upstream primer 3′-terminal deoxycytidine (dC), incoming dCTP/incorporated dCMP, and/or pyrophosphate in the precatalytic (*a* and *b*), partial dCTP incorporation (*c*–*e*), postcatalytic thumb subdomain closed (*f* and *i*), and postcatalytic thumb subdomain open (*g* and *h*) complexes. Spheres represent Ca^{2+} (yellow), Mg^{2+} (green), Mn^{2+} (purple), and Na^+ (purple). (*B*) The dRP lyase active site and locations of reactive water molecules are shown for binary (*a* and *b*), precatalytic (*c* and *d*), partial dCTP incorporation (*e*–*g*), postcatalytic thumb subdomain closed (*h* and *k*), and postcatalytic thumb subdomain open (*i* and *j*) complexes. The binding sites of reactive water molecules X, Y, and Z (red spheres) referred to in Scheme 2 are shown throughout the reaction stages. Electron density F_o–F_c omit maps (cyan; 3σ) are displayed for X, Y, and Z in *B*, *a* and *b*. Dashed lines denote important interactions with distances in angstroms.

modified BER pathway by incorporating the order of the reactions catalyzed by hPolβ (Scheme 1*B*). The interlocking sequence of the two enzymatic activities of hPolβ in the modified BER pathway is further supported by the fact that correct dCTP was incorporated by the polymerase activity with a 17-fold higher efficiency with cross-linked (1.9 $\mu M^{-1}\ s^{-1}$) than uncross-linked (0.11 $\mu M^{-1}\ s^{-1}$) hPolβ (Table 1). The enhanced polymerase efficiency and similarly high fidelity (10^{-5} to 10^{-6}) (Table 1) indicate that it is advantageous to have gap-filling DNA synthesis occurring after Schiff base formation during BER. The modified reaction order is also consistent with the presence of two enzymatic activities within a single polypeptide chain of Polβ, which enables the interlocking mechanism to function optimally. If the reaction order was reversed, the uncross-linked DNA repairing intermediate

would likely dissociate from hPolβ based on a fast DNA dissociation rate of 2.8 s^{-1} (40) and be subsequently damaged by cellular nucleases, leading to genomic instability. Furthermore, the analysis of the full reconstitution of human BER has shown that dRP cleavage by hPolβ is slower than gap-filling DNA synthesis and is actually rate limiting for the entire BER pathway (4). Based on our estimated rates of Schiff base formation (4.5 s^{-1}) and β-elimination (0.31 s^{-1}), we conclude that β-elimination limits overall dRP cleavage by hPolβ and thus, BER. Structurally, the 5′-phosphate of the cross-linked dRP moiety shifted its bound position within the dRP lyase active site over time (*SI Appendix*, Fig. S6 *E* and *F*). In addition, the relatively large distance (6.2 Å) between the C2′ atom and the side chain of E71 (*SI Appendix*, Fig. S2*F*) would require E71 to abstract the C2′ proton via the adjacent water molecule Y (Fig. 4*B*), rather than through direct extraction (see the discussion below). Taking into consideration of the dRP positioning dynamics following Schiff base formation, the requirement for water-mediated C2′ proton abstraction, and the breakage of a strong C-O bond, it is reasonable to conclude that β-elimination has a relatively large energy barrier and is a slow step. In contrast, Schiff base formation is known to be rapid. For example, Schiff base formation in the catalytic cycles of *Thermoplasma acidophilum* transaldolase and fructose-6-phosphate aldolase occurs with rates of 50 to 70 s^{-1} at 30 °C (41). In comparison, Schiff base formation catalyzed by hPolβ is slower but is still about 20-fold faster than β-elimination in the presence or absence of gap-filling DNA synthesis (*SI Appendix*, Fig. S4*O*). Interestingly, the dRP lyase and polymerase activities of hPolβ can be functionally uncoupled in vitro since one of them was active, while the other was not (*SI Appendix*, Figs. S4 and S5). Although the polymerase activity of hPolβ was 17-fold more efficient when it was interlocked with the dRP lyase activity (see above), the latter was insignificantly affected by the former as the dRP lyase displayed comparable activities in the presence or absence of dCTP incorporation (*SI Appendix*, Fig. S4*O*). We acknowledge that our experiments were carried out under specific experimental conditions and cannot exclude results carried out under all possible conditions.

Revising the dRP Lyase Chemical Mechanism. While the ring-closed dRP is more populated at equilibrium compared with the more reactive ring-opened aldehyde form (Scheme 2) (42, 43), it has been hypothesized that either K35 or K72 could facilitate ring opening through protonation of the O4′ atom (*SI Appendix*, Fig. S2 *E* and *F*) of the dRP (11). However, K35-mediated dRP ring opening seems unlikely due to the large distance (6.8 Å) between K35 and the O4′ atom in both $(hPolβ–DNA^{dRP})_A$ and $(hPolβ–DNA^{dRP})_B$ (*SI Appendix*, Fig. S2 *E* and *F*), the structures of the cross-linked intermediate prepared from our second partial BER reconstitution (*SI Appendix*). In contrast, K72, protonated under physiological pH, catalyzed the dRP ring opening, resulting in a deprotonated K72 primed for nucleophilic attack on the aldehyde form of the dRP to yield a Schiff base. Schiff base formation will, in turn, shift the equilibrium from the ring-closed to the ring-opened dRP (44). Moreover, the proximity of Y39 to K72 (3.9 to 4.2 Å) (Fig. 4*B*) in the $hPolβ–DNA^{dRP}$ structures suggests that Y39 may stabilize the deprotonated form of K72 through a hydrogen bond. In addition, water molecule X (Fig. 4*B*) is bound near K72 and should facilitate proton transfer during Schiff base formation. These arguments in combination with the reduced Schiff base seen in the structures of $(hPolβ–DNA^{dRP})_A$ and $(hPolβ–DNA^{dRP})_B$ lead to steps 1 and 2 in the proposed dRP lyase chemical mechanism (Scheme 2).

Following Schiff base formation, the C2′ proton (*SI Appendix*, Fig. S2 *E* and *F*) must be abstracted for β-elimination and release of the dRP cleavage product. Two basic residues in the dRP lyase active site, E26 and E71, have been proposed to perform this abstraction (45). Based on the model of the dRP mimic (*SI Appendix*, Fig. S2 *A*, *ii*) rotated into the dRP lyase active site of $hPolβ–DNA^{THF}$ (*SI Appendix*, Fig. S2*C*), E26 was suggested to be the residue that abstracts the C2′ proton through a bridging water molecule (11). However, both E26 and E71 in all of our cross-linked hPolβ structures (Figs. 2*F* and 4*B*) are far too removed from the C2′ atom to abstract the proton. In addition, E26 does not form any water-mediated contact with C2′ and therefore, likely does not participate in C2′ proton abstraction. On the other hand, water molecule Y is observed bridging E71 and the C2′ atom in all of the cross-linked hPolβ structures (Fig. 4*B*). Thus, we hypothesize that E71 catalyzes the β-elimination reaction through a water-assisted C2′ proton abstraction (step 3 in Scheme 2). Interestingly, there is a water molecule (Z) bound near the 3′-phosphate covalently connected to the dRP moiety (Fig. 4*B*). In this position, water molecule Z can provide a proton and facilitate the β-elimination reaction (step 4 in Scheme 2). Lastly, water molecule Y deprotonated by E71 serves as the nucleophile to hydrolyze and release K72 of hPolβ and HPP (steps 5 and 6 in Scheme 2). Based on these 11 structures of cross-linked hPolβ (Fig. 4*B*), we proposed a detailed chemical mechanism for the dRP lyase activity of hPolβ, including the unexpected water-mediated β-elimination (Scheme 2).

Three Divalent Metal Ions Bound at the Polymerase Active Site of Cross-Linked hPolβ during Catalysis. The pre- and postcatalytic binary structures of cross-linked hPolβ do not possess divalent metal ions bound at the polymerase active site (*SI Appendix*, Fig. S6*J*). In contrast, there are two divalent metal ions at the A and B sites in the precatalytic ternary structure $(hPolβ–DNA^{dRP}•dNTP)_2$ and three divalent metal ions at the A, B, and C sites in the late reaction-state structures (Fig. 4 *A*, *e*, *f*, and *i*). Unlike $(hPolβ–DNA^{dRP}•dNTP)_2$, the precatalytic ternary structure $(hPolβ–DNA^{dRP}•dNTP)_1$ has Na^+ bound at the A site and Ca^{2+} at the B site (Fig. 4 *A*, *a*). The modeling of the A-site metal ion as Na^+ is also reminiscent of postcatalytic structures, wherein the coordination ligand 3′-OH is lost and the Mg^{2+} is replaced with Na^+ (18, 23). In the $(hPolβ–DNA^{dRP}•dNTP)_1$ structure, the upstream primer terminus 3′-OH is facing away and far (5.4 Å) from the Pα of dCTP, and therefore, it is considered to be a nonproductive conformation; however, in $(hPolβ–DNA^{dRP}•dNTP)_2$, the 3′-OH is pointing toward and close to (3.7 Å) the Pα of dCTP, and the ternary structure is considered to be the productive conformation (Fig. 3*E*). When both Ca^{2+} ions at the A and B sites were replaced by Mg^{2+}, the phosphodiester bond formation is initiated and accompanied by the appearance of Mg^{2+} at the C site (Fig. 4*A*). Interestingly, only the C-site metal ion is dynamic based on its repositioning by at least 0.6 Å during phosphodiester bond formation (Fig. 3*G*). The dynamic nature of the C-site Mg^{2+} has also been observed with uncross-linked hPolβ during catalysis (23). As proposed previously (23, 34, 46, 47), the simultaneous appearance of the C-site Mg^{2+} with phosphodiester bond formation may imply that the C-site Mg^{2+} neutralizes the negative charge developed in the transition state and thereby, facilitates phosphodiester bond formation. The C-site Mg^{2+} may also act to stabilize the product state in order to prevent pyrophosphorolysis (48, 49). Regardless, cross-linked hPolβ, as uncross-linked DNA polymerases (18, 20–23, 34, 35, 47), follows the "three–metal ion mechanism" rather than the "two–metal ion mechanism" (50) for catalysis.

Effect of the Cross-Link between hPolβ and DNA on Nucleotide Binding and Incorporation Kinetics. Although the cross-link decreased k_p of correct dCTP by 4-fold, it lowered its K_d by 68-fold, leading to a 17-fold higher gap-filling DNA synthesis efficiency (Table 1). Relative to uncross-linked hPolβ, the cross-link has a larger kinetic effect on K_d over k_p (Table 1). Structurally, the cross-link stabilizes the templating dG by anchoring the entire DNA

substrate, leading to both stronger stacking of dCTP with the 3′-terminal nucleotide of the upstream primer and the shortened hydrogen bonds within the nascent base pair by 0.3 to 0.5 Å in the hPolβ–DNA^{dRP}•dCTP structures (Fig. 3 *A*–*C*). Additionally, several hydrogen bonds between polymerase active site residues and dCTP were also shortened by 0.1 to 0.3 Å in the hPolβ–DNA^{dRP}•dNTP structures relative to the uncross-linked hPolβ•DNA^{P}•dNTP structure. Together, these factors structurally contribute to the tighter binding of correct dCTP to cross-linked over uncross-linked hPolβ. However, the higher active site stability in hPolβ–DNA^{dRP}•dNTP over hPolβ•DNA^{P}•dNTP may slow down the rate-limiting protein conformational change step in a general kinetic mechanism for DNA polymerases (51, 52), leading to slower dNTP incorporation by the cross-linked hPolβ. Furthermore, cross-linked hPolβ can form two different ternary complexes [(hPolβ–DNA^{dRP}•dNTP)$_1$ and (hPolβ–DNA^{dRP}•dNTP)$_2$] (Fig. 3 *B* and *C*). The former, unlike the latter and all reaction-state structures (Figs. 3 *E* and *G* and 4*A*), possesses a nonproductive polymerase active site (see above). If the ternary complex of cross-linked hPolβ was partially trapped in the nonproductive state (hPolβ–DNA^{dRP}•dNTP)$_1$, which slowly isomerized to (hPolβ–DNA^{dRP}•dNTP)$_2$, the overall rate of the gap-filling DNA synthesis by cross-linked hPolβ would be decreased. Together, the two aforementioned kinetic factors likely contribute to the fourfold-lower k_p value with cross-linked over uncross-linked hPolβ.

In summary, we utilized two partial BER reconstitution assays, X-ray crystallography, and presteady-state kinetics to thoroughly investigate the effect of the cross-link between hPolβ and DNA via Schiff base formation on the polymerase and dRP lyase activities. Transient imino complexes between hPolβ and DNA containing a natural 5′-dRP were captured by $NaBH_4$ reduction and crystallized. Current experiments indicated that gap-filling DNA synthesis took place after Schiff base formation but before β-elimination. Our unanticipated biochemical, MS, structural, and kinetic results prompted us to revise the dRP lyase chemical mechanism (Scheme 2) and propose the modified BER pathway (Scheme 1*B*). Like uncross-linked hPolβ, cross-linked hPolβ also employed the three–metal ion mechanism for phosphodiester bond formation. This work significantly advances our understanding of the two enzymatic activities of hPolβ and their roles in BER. Furthermore, overexpression of hPolβ messenger RNA has been associated with various cancer types, whereas deficiencies in Polβ result in hypersensitivity to alkylating agents, induced apoptosis, and chromosomal breaking (53–56). Approximately 30% of human tumors examined for mutations in hPolβ appear to express hPolβ variant proteins (57–59). The Y265C mutation in Polβ causes lupus in mice (60). Thus, hPolβ has been targeted for chemotherapeutic intervention of cancer and other disorders (61), and our in-depth study of the enzymatic activities of hPolβ should facilitate such drug development efforts.

Materials and Methods

The First Partial BER Reconstitution Assay. The purified 12-mer (5′-GTGCTGATGCGC-3′) and 19-mer (5′-UGTCGGACGGCTGTGGGTC-3′; U: 2′-deoxyuridine) were individually 5′ radiolabeled for 30 min at 25 °C by Optikinase in the presence of [γ-^{32}P]–adenosine triphosphate. A nicked DNA substrate (DNA1^{N}) was formed by annealing the unlabeled template 31-mer (5′-GACCCAGACGCGTCCGACGGCGCATCAGCAC-3′) with the [^{32}P]-labeled upstream primer 12-mer and the downstream 19-mer. The doubly [^{32}P]-labeled DNA1^{N} (10 nM) was treated with UDG (40 nM) for 30 min prior to reacting with hPolβ (200 nM) in the presence of dCTP (0, 1, or 100 μM) in the reaction buffer (50 mM tris(hydroxymethyl)aminomethane [Tris]·HCl, pH 7.8, 5 mM $MgCl_2$, 50 mM NaCl, 0.1 mM EDTA, 5 mM dithiothreitol, 10% glycerol, 0.1 mg/mL of bovine serum albumin) at 25 °C. Notably, DNA1^{N} was processed by UDG to generate DNA1^{dRP} containing a freshly produced abasic site. The reaction between DNA1^{dRP} and hPolβ with dCTP was carried out in a rapid chemical quench apparatus RQF-3 (Kintek Corp.) and quenched after various times by 0.37 M EDTA. The quenched reaction mixtures were collected in microcentrifuge tubes containing $NaBH_4$ (100 mM), which reduced and trapped cross-linked hPolβ–DNA complexes. The reaction mixtures, in identical volumes, were loaded and analyzed via both a urea-based polyacrylamide gel electrophoresis (PAGE) sequencing gel and an SDS-PAGE gel to resolve DNA polymerization and the cross-linked hPolβ–DNA products, respectively. The [^{32}P]-labeled products were quantified using a Typhoon TRIO (GE Healthcare) and ImageQuant (Molecular Dynamics). The plots of each product or the remaining 19-mer concentrations vs. early reaction times were fit to different equations to obtain corresponding rate constants (*SI Appendix*).

Identification of Cross-Linked hPolβ–DNA Products by Using Liquid Chromatography with Tandem Mass Spectrometry. The 0.256- and 20-s reduced reaction mixtures were separated via SDS-PAGE, and the hPolβ–DNA gel bands were sliced. The sliced gel pieces were washed with buffer (50% acetonitrile [ACN] in 2 mg/mL NH_4HCO_3) thrice. The washed gel slices were dehydrated by adding 100% ACN and resuspended in 30 μL of 50 mM NH_4HCO_3. Tris(2-carboxyethyl)phosphine (5 mM) was added for reduction, and the mixture was incubated at 55 °C for 20 min. The remaining reducing agent was removed, and the gel slices were alkylated by adding 10 mM iodoacetamide and incubated in the dark at room temperature for 20 min. The alkylated gel slices were dehydrated by adding 100% ACN. One microgram of trypsin in 30 μL of 50 mM NH_4HCO_3 was added to the mix and incubated in a thermomixer at 600 rpm and 37 °C for 3 h. Digested peptides were eluted from the gel slices by vigorous vortexing in 50% ACN. Eluate was freeze dried and resuspended in 20 μL of 0.1% formic acid for LC-MS/MS (liquid chromatography with tandem mass spectrometry) analysis.

For the LC-MS/MS analysis, a Thermo Q Exactive HF (high-resolution electrospray tandem mass spectrometer) was used in conjunction with the Dionex UltiMate 3000 RSLCnano System. A 2-μL sample was loaded onto a trap column (Thermo μ-Precolumn 5 mm with nanoViper tubing 30-μm inner dimension × 10 cm). The flow rate was 300 nl/min for separation on an analytical column (Acclaim PepMap RSLC 75 μm × 15 cm nanoviper). Mobile phase A was composed of 99.9% H_2O (EMD Omni Solvent) and 0.1% formic acid, while mobile phase B had 99.9% ACN and 0.1% formic acid. A 90-min linear gradient from 3 to 45% B was performed. During the chromatographic separation, the Q Exactive HF was operated in a data-dependent mode and under direct control of the Thermo Excalibur 3.1.66. The MS data were acquired using the following parameters: 20 data-dependent collision-induced dissociation MS/MS scans per full scan (350 to 1,700 *m/z*) at 60,000 resolution. MS2 (fragment ion spectra from a second stage of mass spectrometry in tandem mass spectrometry) was acquired in centroid mode at 15,000 resolution. Ions with single charge or charges more than seven as well as unassigned charge were excluded. A 15-s dynamic exclusion window was used.

For data analysis, resultant raw files were searched against the protein sequence of hPolβ by using the Mascot search engine (SwissProt database; restricted to *Homo sapiens*) in error-tolerant mode to identify the peptides and the modifications. No decoy database was used as that is incompatible with the Error-Tolerant search.

Data Availability. Atomic coordinates and structure factors for the reported crystal structures have been deposited in Protein Data Bank (ID codes 7RBE, 7RBF, 7RBG, 7RBH, 7RBI, 7RBJ, 7RBK, 7RBL, 7RBM, 7RBN, and 7RBO). All other data are included in the manuscript and/or *SI Appendix*.

ACKNOWLEDGMENTS. This work was supported by NIH Grants R35GM140819 (to S.M.H.) and R01GM122093 (to Z.S.). This research used resources of the Advanced Photon Source of the Argonne National Laboratory under Contract DE-AC02-06CH11357. Use of the Lilly Research Laboratories Collaborative Access Team beamline at Sector 31 of the Advanced Photon Source was provided by Eli Lilly & Company. We thank the Translational Science Laboratory at Florida State University (FSU) for performing the MS/MS analysis and the FSU Institute of Molecular Biophysics at FSU for providing us access to the Nanotemper microscale thermophoresis instrument.

1. G. L. Dianov, U. Hübscher, Mammalian base excision repair: The forgotten archangel. *Nucleic Acids Res.* **41**, 3483–3490 (2013).
2. T. L. Scott, S. Rangaswamy, C. A. Wicker, T. Izumi, Repair of oxidative DNA damage and cancer: Recent progress in DNA base excision repair. *Antioxid. Redox Signal.* **20**, 708–726 (2014).
3. S. S. Wallace, Base excision repair: A critical player in many games. *DNA Repair (Amst.)* **19**, 14–26 (2014).
4. D. K. Srivastava *et al.*, Mammalian abasic site base excision repair. Identification of the reaction sequence and rate-determining steps. *J. Biol. Chem.* **273**, 21203–21209 (1998).

5. J. Nakamura, J. A. Swenberg, Endogenous apurinic/apyrimidinic sites in genomic DNA of mammalian tissues. *Cancer Res.* **59**, 2522–2526 (1999).
6. M. García-Díaz, K. Bebenek, T. A. Kunkel, L. Blanco, Identification of an intrinsic 5′-deoxyribose-5-phosphate lyase activity in human DNA polymerase lambda: A possible role in base excision repair. *J. Biol. Chem.* **276**, 34659–34663 (2001).
7. Y. Matsumoto, K. Kim, Excision of deoxyribose phosphate residues by DNA polymerase beta during DNA repair. *Science* **269**, 699–702 (1995).
8. C. E. Piersen, R. Prasad, S. H. Wilson, R. S. Lloyd, Evidence for an imino intermediate in the DNA polymerase beta deoxyribose phosphate excision reaction. *J. Biol. Chem.* **271**, 17811–17815 (1996).
9. R. Prasad, W. A. Beard, P. R. Strauss, S. H. Wilson, Human DNA polymerase beta deoxyribose phosphate lyase. Substrate specificity and catalytic mechanism. *J. Biol. Chem.* **273**, 15263–15270 (1998).
10. R. Prasad *et al.*, Functional analysis of the amino-terminal 8-kDa domain of DNA polymerase beta as revealed by site-directed mutagenesis. DNA binding and 5′-deoxyribose phosphate lyase activities. *J. Biol. Chem.* **273**, 11121–11126 (1998).
11. R. Prasad *et al.*, Structural insight into the DNA polymerase beta deoxyribose phosphate lyase mechanism. *DNA Repair (Amst.)* **4**, 1347–1357 (2005).
12. W. W. Duym, K. A. Fiala, N. Bhatt, Z. Suo, Kinetic effect of a downstream strand and its 5′-terminal moieties on single nucleotide gap-filling synthesis catalyzed by human DNA polymerase lambda. *J. Biol. Chem.* **281**, 35649–35655 (2006).
13. C. E. Piersen, A. K. McCullough, R. S. Lloyd, AP lyases and dRPases: Commonality of mechanism. *Mutat. Res.* **459**, 43–53 (2000).
14. L. J. Deterding, R. Prasad, G. P. Mullen, S. H. Wilson, K. B. Tomer, Mapping of the 5′-2-deoxyribose-5-phosphate lyase active site in DNA polymerase beta by mass spectrometry. *J. Biol. Chem.* **275**, 10463–10471 (2000).
15. Y. Matsumoto, K. Kim, D. S. Katz, J. A. Feng, Catalytic center of DNA polymerase beta for excision of deoxyribose phosphate groups. *Biochemistry* **37**, 6456–6464 (1998).
16. M. R. Sawaya, R. Prasad, S. H. Wilson, J. Kraut, H. Pelletier, Crystal structures of human DNA polymerase beta complexed with gapped and nicked DNA: Evidence for an induced fit mechanism. *Biochemistry* **36**, 11205–11215 (1997).
17. Z. Wang, X. Wu, E. C. Friedberg, Molecular mechanism of base excision repair of uracil-containing DNA in yeast cell-free extracts. *J. Biol. Chem.* **272**, 24064–24071 (1997).
18. B. D. Freudenthal, W. A. Beard, D. D. Shock, S. H. Wilson, Observing a DNA polymerase choose right from wrong. *Cell* **154**, 157–168 (2013).
19. D. D. Shock, B. D. Freudenthal, W. A. Beard, S. H. Wilson, Modulating the DNA polymerase β reaction equilibrium to dissect the reverse reaction. *Nat. Chem. Biol.* **13**, 1074–1080 (2017).
20. A. J. Reed, Z. Suo, Time-dependent extension from an 8-oxoguanine lesion by human DNA polymerase beta. *J. Am. Chem. Soc.* **139**, 9684–9690 (2017).
21. A. M. Whitaker, M. R. Smith, M. A. Schaich, B. D. Freudenthal, Capturing a mammalian DNA polymerase extending from an oxidized nucleotide. *Nucleic Acids Res.* **45**, 6934–6944 (2017).
22. B. D. Freudenthal *et al.*, Uncovering the polymerase-induced cytotoxicity of an oxidized nucleotide. *Nature* **517**, 635–639 (2015).
23. R. Vyas, A. J. Reed, E. J. Tokarsky, Z. Suo, Viewing human DNA polymerase β faithfully and unfaithfully bypass an oxidative lesion by time-dependent crystallography. *J. Am. Chem. Soc.* **137**, 5225–5230 (2015).
24. J. A. Brown, W. W. Duym, J. D. Fowler, Z. Suo, Single-turnover kinetic analysis of the mutagenic potential of 8-oxo-7,8-dihydro-2′-deoxyguanosine during gap-filling synthesis catalyzed by human DNA polymerases lambda and beta. *J. Mol. Biol.* **367**, 1258–1269 (2007).
25. W. A. Beard, D. D. Shock, V. K. Batra, L. C. Pedersen, S. H. Wilson, DNA polymerase beta substrate specificity: Side chain modulation of the "A-rule." *J. Biol. Chem.* **284**, 31680–31689 (2009).
26. Y. J. Lee *et al.*, Identification and biosynthesis of thymidine hypermodifications in the genomic DNA of widespread bacterial viruses. *Proc. Natl. Acad. Sci. U.S.A.* **115**, E3116–E3125 (2018).
27. J. E. DeNizio, M. Y. Liu, E. M. Leddin, G. A. Cisneros, R. M. Kohli, Selectivity and promiscuity in TET-mediated oxidation of 5-methylcytosine in DNA and RNA. *Biochemistry* **58**, 411–421 (2019).
28. J. A. Brown, L. R. Pack, L. E. Sanman, Z. Suo, Efficiency and fidelity of human DNA polymerases λ and β during gap-filling DNA synthesis. *DNA Repair (Amst.)* **10**, 24–33 (2011).
29. J. A. Brown, L. R. Pack, J. D. Fowler, Z. Suo, Presteady state kinetic investigation of the incorporation of anti-hepatitis B nucleotide analogues catalyzed by noncanonical human DNA polymerases. *Chem. Res. Toxicol.* **25**, 225–233 (2012).
30. B. G. Werneburg *et al.*, DNA polymerase beta: Pre-steady-state kinetic analysis and roles of arginine-283 in catalysis and fidelity. *Biochemistry* **35**, 7041–7050 (1996).
31. P. B. Balbo, E. C. Wang, M. D. Tsai, Kinetic mechanism of active site assembly and chemical catalysis of DNA polymerase β. *Biochemistry* **50**, 9865–9875 (2011).
32. M. Figiel *et al.*, Coordination between the polymerase and RNase H activity of HIV-1 reverse transcriptase. *Nucleic Acids Res.* **45**, 3341–3352 (2017).
33. W. A. Beard, S. H. Wilson, Structure and mechanism of DNA polymerase β. *Biochemistry* **53**, 2768–2780 (2014).
34. T. Nakamura, Y. Zhao, Y. Yamagata, Y. J. Hua, W. Yang, Watching DNA polymerase η make a phosphodiester bond. *Nature* **487**, 196–201 (2012).
35. J. A. Jamsen *et al.*, Time-lapse crystallography snapshots of a double-strand break repair polymerase in action. *Nat. Commun.* **8**, 253 (2017).
36. J. C. Fromme, S. D. Bruner, W. Yang, M. Karplus, G. L. Verdine, Product-assisted catalysis in base-excision DNA repair. *Nat. Struct. Biol.* **10**, 204–211 (2003).
37. B. Sun, K. A. Latham, M. L. Dodson, R. S. Lloyd, Studies on the catalytic mechanism of five DNA glycosylases. Probing for enzyme-DNA imino intermediates. *J. Biol. Chem.* **270**, 19501–19508 (1995).
38. A. T. Raper, B. A. Maxwell, Z. Suo, Dynamic processing of a common oxidative DNA lesion by the first two enzymes of the base excision repair pathway. *J. Mol. Biol.* **433**, 166811 (2021).
39. Y. Lai, Y. Weizmann, Y. Liu, The deoxyribose phosphate lyase of DNA polymerase β suppresses a processive DNA synthesis to prevent trinucleotide repeat instability. *Nucleic Acids Res.* **46**, 8940–8952 (2018).
40. B. J. Vande Berg, W. A. Beard, S. H. Wilson, DNA structure and aspartate 276 influence nucleotide binding to human DNA polymerase beta. Implication for the identity of the rate-limiting conformational change. *J. Biol. Chem.* **276**, 3408–3416 (2001).
41. V. Sautner, M. M. Friedrich, A. Lehwess-Litzmann, K. Tittmann, Converting transaldolase into aldolase through swapping of the multifunctional acid-base catalyst: Common and divergent catalytic principles in F6P aldolase and transaldolase. *Biochemistry* **54**, 4475–4486 (2015).
42. M. Manoharan *et al.*, The characterization of abasic sites in DNA heteroduplexes by site specific labeling with carbon-13. *J. Am. Chem. Soc.* **110**, 1620–1622 (1988).
43. J. A. Wilde, P. H. Bolton, A. Mazumder, M. Manoharan, J. A. Gerlt, Characterization of the equilibrating forms of the aldehydic abasic site in duplex DNA by 17O-NMR. *J. Am. Chem. Soc.* **111**, 1894–1896 (1989).
44. S. M. Daskalova, X. Bai, S. M. Hecht, Study of the lyase activity of human DNA polymerase β using analogues of the intermediate Schiff base complex. *Biochemistry* **57**, 2711–2722 (2018).
45. J. A. Feng, C. J. Crasto, Y. Matsumoto, Deoxyribose phosphate excision by the N-terminal domain of the polymerase beta: The mechanism revisited. *Biochemistry* **37**, 9605–9611 (1998).
46. A. J. Reed, R. Vyas, A. T. Raper, Z. Suo, Structural insights into the post-chemistry steps of nucleotide incorporation catalyzed by a DNA polymerase. *J. Am. Chem. Soc.* **139**, 465–471 (2017).
47. Y. Gao, W. Yang, Capture of a third Mg^{2+} is essential for catalyzing DNA synthesis. *Science* **352**, 1334–1337 (2016).
48. L. Perera *et al.*, Requirement for transient metal ions revealed through computational analysis for DNA polymerase going in reverse. *Proc. Natl. Acad. Sci. U.S.A.* **112**, E5228–E5236 (2015).
49. L. Perera, B. D. Freudenthal, W. A. Beard, L. G. Pedersen, S. H. Wilson, Revealing the role of the product metal in DNA polymerase β catalysis. *Nucleic Acids Res.* **45**, 2736–2745 (2017).
50. L. S. Beese, T. A. Steitz, Structural basis for the 3′-5′ exonuclease activity of Escherichia coli DNA polymerase I: A two metal ion mechanism. *EMBO J.* **10**, 25–33 (1991).
51. A. T. Raper, A. A. Stephenson, Z. Suo, Sharpening the scissors: Mechanistic details of CRISPR/Cas9 improve functional understanding and inspire future research. *J. Am. Chem. Soc.* **140**, 11142–11152 (2018).
52. Y. C. Tsai, K. A. Johnson, A new paradigm for DNA polymerase specificity. *Biochemistry* **45**, 9675–9687 (2006).
53. D. K. Srivastava, I. Husain, C. L. Arteaga, S. H. Wilson, DNA polymerase beta expression differences in selected human tumors and cell lines. *Carcinogenesis* **20**, 1049–1054 (1999).
54. Y. Canitrot *et al.*, Overexpression of DNA polymerase beta in cell results in a mutator phenotype and a decreased sensitivity to anticancer drugs. *Proc. Natl. Acad. Sci. U.S.A.* **95**, 12586–12590 (1998).
55. V. Bergoglio *et al.*, Deregulated DNA polymerase beta induces chromosome instability and tumorigenesis. *Cancer Res.* **62**, 3511–3514 (2002).
56. V. Bergoglio *et al.*, Enhanced expression and activity of DNA polymerase beta in human ovarian tumor cells: Impact on sensitivity towards antitumor agents. *Oncogene* **20**, 6181–6187 (2001).
57. T. Lang, S. Dalal, A. Chikova, D. DiMaio, J. B. Sweasy, The E295K DNA polymerase beta gastric cancer-associated variant interferes with base excision repair and induces cellular transformation. *Mol. Cell. Biol.* **27**, 5587–5596 (2007).
58. D. Starcevic, S. Dalal, J. B. Sweasy, Is there a link between DNA polymerase beta and cancer? *Cell Cycle* **3**, 998–1001 (2004).
59. S. S. Lange, K. Takata, R. D. Wood, DNA polymerases and cancer. *Nat. Rev. Cancer* **11**, 96–110 (2011).
60. A. G. Senejani *et al.*, Mutation of POLB causes lupus in mice. *Cell Rep.* **6**, 1–8 (2014).
61. A. S. Jaiswal *et al.*, DNA polymerase β as a novel target for chemotherapeutic intervention of colorectal cancer. *PLoS One* **6**, e16691 (2011).